How do Laboratory Friction Parameters Compare With Observed Fault Slip and Geodetically Derived Friction Parameters? Insights From the Longitudinal Valley Fault, Taiwan

S. A. M. den Hartog, Marion Y. Thomas, D. R. Faulkner

How do laboratory friction parameters compare with observed fault slip and geodetically derived friction parameters? Insights from the Longitudinal Valley Fault, Taiwan

S. A. M. den Hartog[1†], M. Y. Thomas[2], and D. R. Faulkner[1]

[1] Rock Deformation Laboratory, School of Environmental Sciences, University of Liverpool, Liverpool, United Kingdom.

[2] Institut des Sciences de la Terre de Paris, CNRS-UMR 7193, Sorbonne Université, Paris, France.

Corresponding author: Sabine den Hartog (s.den_hartog@hw.ac.uk)

†Now at: The Lyell Centre, Heriot-Watt University, Edinburgh, UK.

Key Points:

- Laboratory-determined frictional parameters are compared with those obtained geodetically and with observed fault slip behaviour
- Derived friction parameters correspond well with each other and are distinctive for creeping and partially locked sections of the fault
- Upscaling of laboratory meaurements of fault frictional properties reflects the large-scale slip behaviour of faults well

Abstract

Laboratory measurements of constitutive frictional parameters are commonly inferred to explain the wide variety of slip behaviour seen on natural faults. The extent to which these small-scale measurements directly relate to fault slip behaviour remains obscure. In this work we compare laboratory-determined frictional parameters on surface-derived samples from along the length of the Longitudinal Valley Fault (LVF) in Taiwan with the observed slip behaviour and with frictional parameters obtained geodetically. The LVF displays partially locked and creeping sections and a M_w 6.8 event in 2003 produced transient acceleration of slip in the adjacent creeping sections that can be used to determine the frictional parameters for direct comparison with the laboratory-measured ones. We find that the laboratory-measured friction parameters are markedly different for samples collected from the creeping and partially locked sections of the fault, the former showing lower friction coefficients and more positive values of the fault stability parameter (a-b). Moreover, values for the product of (a-b) and the effective normal stress, determined geodetically, relate very closely to those measured in the laboratory. Mineralogical and microstructural analyses of the fault gouges show that some mineralogically similar gouges produce distinctly different frictional behaviour, and that this may be related to the presence and distribution of kaolinite. We conclude overall that upscaling of laboratory measurements of fault frictional properties appears to reflect well the large-scale slip behaviour of faults.

Plain Language Summary

Tectonic faults contained within the Earth's crust can sometimes slip in continuous slow steady motion, known as “creep”. They can also sometimes slip in a more episodic fashion, during earthquakes, and stay locked the rest of the time. Both behaviours result in different surface movement, quantifiable via geodetic methods. Models of fault slip behaviour typically rely on data derived from laboratory friction measurements on rocks from fault zones. However, it is unclear whether the small-scale laboratory measurements directly relate to observed large-scale fault behaviour.

Here, we used fault rock samples from the Longitudinal Valley Fault (LVF) in Taiwan to compare the results from laboratory measurements with the slip behaviour and inferred frictional properties from geodetic observations. Samples were taken both from the partially locked and creeping parts of the fault. We performed laboratory measurements on these samples that yield results that correctly predict either earthquake slip or creep. We also used the geodetic measurements of the LVF to derive the same parameters that are measured in the laboratory and find they compare well. We conclude that small-scale laboratory measurements indeed reflect the intrinsic frictional properties of the LVF that result in the observed large-scale behaviour of this major tectonic fault.

1 Introduction

The range of fault frictional constitutive properties determined from laboratory experiments are commonly considered to explain the wide variety of fault slip behaviour, from fault creep, through episodic slow slip events, to regular earthquakes (e.g. Bürgmann, 2018; Den Hartog et al., 2012; Dublanchet et al., 2013; Faulkner et al., 2003; Hillers & Wesnousky, 2008; Thomas et al., 2017). While the direct link between laboratory measured frictional properties and fault behaviour is often inferred, it has rarely been explicitly tested (Johnson et al., 2006). This

omission is partly due to finding a suitable example of a large fault from which samples can be recovered and measured in the laboratory and their constitutive parameters compared with a varied slip behaviour observed over several years. Strong spatial variations of slip mode have been observed along subduction zones (e.g. Chlieh et al., 2008; Cross & Freymueller, 2007; Hyndman et al., 1997; Métois et al., 2012; Ozawa et al., 2012; Pritchard & Simons, 2006; Wallace et al., 2004) and on some continental faults (Bürgmann et al., 2000; Jolivet et al., 2012; Murray et al., 2001; Rousset et al., 2016; Thomas et al., 2014a; Titus et al., 2006), but extensive sample recovery in these environments is often problematic.

A good example of a continental fault that displays varied slip behaviour is the Longitudinal Valley Fault (LVF), which runs parallel to the east coast of Taiwan and marks the suture between the Eurasian and Philippine Sea Plate (Lee et al., 1998; Figure 1a). It accommodates reverse-left lateral motion, creeps near the surface (e.g. Angelier et al., 1997) but has also produced $M_w > 6.8$ earthquakes, including 4 events in 1951 (Shyu et al., 2007) and the M_w 6.8 Chengkung earthquake of 2003 (e.g. Wu et al., 2006). The spatial and temporal variation of fault motion on the LVF determined geodetically provides a rare opportunity to compare geodetically-determined friction parameters with laboratory-measured frictional parameters of samples collected along its length. If they are comparable, it will provide a strong indication that the latter can be used to predict its range of behaviour from fault creep to seismic slip.

The variations in laboratory-derived fault constitutive parameters, and hence inferred fault slip behaviour, is thought to be related to variations in fluid pressure, effective normal stress, but in particular to mineralogical variations, notably clay content (e.g. Den Hartog & Spiers, 2013; Ikari et al., 2011). Clay-rich fault rocks typically show pronounced velocity-strengthening characteristics that are associated with fault creep. Clay-poor fault rocks are velocity-weakening - a prerequisite for unstable earthquake slip. In subduction zones, the systematic changes in pressure and temperature with depth promote clay mineral diagenesis which is inferred to explain frictional stability changes and the extent of the seismogenic zone (e.g. Den Hartog et al., 2013; Moore et al., 2007). In the case of the LVF, the link between mineralogy and slip behavior needs testing as the mineralogy of the fault-bounding Lichi mélange along the southern creeping section was found to be similar to that of the volcanoclastic formations that bound the fault in the partially locked northern section (Thomas et al., 2014b). Hence, it is currently not clear what might control the variation in slip mode along the LVF.

Surface strain adjacent to the LVF over the last three decades is well documented from campaign mode and continuous GPS, levelling data and InSAR (e.g. Champenois et al., 2012; Chen et al., 2012; Lee et al., 2005; Yu & Kuo, 2001). This wealth of data and analysis provides an outstanding opportunity to study the factors that control the seismic and aseismic fault sections near the surface. Here we go one step further and perform laboratory friction measurements on samples from the LVF collected and described by Thomas et al. (2014b) and compare the results with geodetic and seismological observations on fault rheology along the LVF (Thomas et al., 2014a; Thomas et al., 2017). We thus offer a comprehensive comparison between laboratory-derived properties of surface-derived samples, their mineralogy, and the observed geodetic behaviour of an active fault system that is rarely achieved.

2 The Longitudinal Valley Fault in Taiwan: Tectonic setting

The LVF borders the Coastal Range in Taiwan (Figure 1a), which results from the accretion of the Luzon Arc and its forearc basin to the exhumed metamorphic basement of

passive Chinese continental margin during the arc-continent collision in the last 7 m.y. (Huang et al., 2006; Liu et al., 2000; Suppe, 1984; Teng, 1981). With regard to the geology, five rock units can be distinguished in the Coastal Range. The Tuluanshan Arc Formation and the Fanshuliao volcanoclastic deposits are pre-collision island–arc lithofacies, whereas the Paliwan lithic flysch, the Peinanshan and Wuho conglomerates (molasse), and the Lichi mélange are later syn/post-collision lithofacies (Figure 1a). The accreted Miocene-Pliocene volcanic islands that form the Tuluanshan Formation are distributed all along the Coastal Range and they usually form mountain ridges, covering over 1/3 of the area. The Paliwan and the Fanshuliao Formations correspond to the remnant of forearc and intra-arc basins. They are subdivided in two stratigraphic layers to reflect the variation of sedimentary sources with time. The late Miocene to early Pliocene Fanshuliao Formation, conformably overlies the Tuluanshan volcanics with a slight interfingering contact. The arc islands seems to have been the major source of these sedimentary rocks, with some contribution from the non-metamorphic cover sequences of the proto-Taiwan island (Teng et al., 1988). The Plio-Pleistocene Paliwan Formation conformably overlies both the Fanshuliao and the Tuluanshan Formations. Its mineralogical content favours a more predominant contribution of the low-grade metamorphic exposed Central Range, over the one from the arc-islands, as a source for the sedimentary deposits. The Lichi Formation, which crops out with variable thickness (up to ~ 2 km) on the western side of the Coastal Range (Figure 1a), is a characteristic block-in-matrix mélange with an argillaceous matrix that displays slickensided surfaces. The exotic blocks inside the Lichi mélange vary in size (millimeters to kilometers) and lithology. Arc products (from the Luzon arc), ophiolites, and sedimentary rocks can be found. The origin of the Lichi mélange has been highly debated (see Thomas et al., 2014b for a thorough discussion). Here, we favour a tectonic collision origin, where the protolith of the mélange is the forearc basin (Fanhsuliao), and the exotic blocks have been incorporated during the early stage of the collision. A detailed description of the mineralogical contents of each formation, together with a more exhaustive bibliography can be found in Thomas et al. (2014b).

3 Methods

3.1 Experimental methods

3.1.1 Sample material

Two field surveys and one core sampling from shallow drilling have been conducted to study the different units of the Coastal Range. A total of 73 samples were collected (Thomas et al, 2014b). For this study, we selected five field samples (Figure 1b, Table 1), 3 from the partially locked section (LVF1, LVF21, LVF34) and two from the creeping section (LVF4 and LVF22). LVF1 and LVF34 are from a section of the LVF that is overall creeping, but these samples were collected within an area that was inferred to be partially locked based on the geodetic analysis (Figure 1b and 1d). Using mineralogical and structural analysis they were assigned to the Paliwan and Fanshuliao Formations, respectively (cf. Section 2). LVF21 also is from the Paliwan Formation, but sampled further north. LVF4 and LVF22 are both from the Lichi mélange. Sample LVF4, in particular, was collected within the exhumed part of the fault gouge and compared, using an electron probe micro-analyzer, with a borehole core sample collected a few cm away from the fault. They both showed similar microstructures and mineral phases (Thomas et al., 2014b). Moreover, none of the 73 collected samples showed much evidence for metamorphism in agreement with the shallow exhumation (less than 2 km) (Shyu et

al., 2006) and relatively cold conditions (temperature less than 450°C in the 0–30 km depth range) inferred from the thermokinematic modeling of Simoes et al. (2007). Consequently, the samples collected within the exhumed fault zone are likely representative of the ongoing deformation along the LVF at a relatively shallow depth (a few kilometers). Finally, for comparison purposes (see Discussion), we also used the KGa-1b kaolinite standard from the Clay Minerals Society and a mixture of LVF21 and KGa-1b.

Table 1. List of samples used in this study, including their location, the formation they were taken from and their composition. Qtz = quartz, Plag = plagioclase, K-fsp = K-feldspar, Calc = Calcite, Mus/ill = muscovite/illite, Chl = chlorite, Kao = kaolinite.

Sample	**Location**	**Formation**	**Fault section**	**Composition**						
				Qtz	**Plag**	**K-fsp**	**Calc**	**Mus/ill**	**Chl**	**Kao**
LVF1	23°29’11” N 121°23’58” W	Paliwan	Locked	43	16	3	2	27	9	0
LVF4	23°10’5” N 121°14’44” W	Lichi	Creeping	33	14	4	0	31	8	11
LVF21	23°38’51” N 121°27’40” W	Paliwan	Locked	28	13	3	0	43	14	0
LVF22	23°3’7” N 121°12’12” W	Lichi	Creeping	32	16	2	0	30	9	12
LVF34	23°29’6” N 121°24’18” W	Fanshuliao	Locked	59	16	2	3	15	5	0
KGa-1b[a]	N.A.	N.A.	N.A.							96
88:12 LVF21:KAO	N.A.	N.A.	N.A.	24	11	3	0	37	12	12

Note. [a]Obtained from the Clay Minerals Society. [b]LVF21 and KGa-1b mixed by weight in proportion 88:12.

With regard to the preparation of the samples, the tendency of clays to flocculate implies that sieving them usually leads to a predominance of a smaller grain size than the sieve opening size. We therefore focused on a consistent preparation method rather than a sieving size. After using a hammer to generate mm-sized particles, we crushed each sample for up to 5 seconds in a steel disk mill. The sample powders were subsequently treated in a Retsch PM100 ball mill with agate jar, at 400 rpm for 5 minutes. We finally sieved the samples at 250 μm to test for the presence of anomalously large pieces. Inspection of one of the samples (LVF1) showed that this procedure resulted in a powder of which virtually all particles passed through a 125 μm sieve.

A small fraction of each sample was next treated for XRD analysis by wet crushing in a McCrone mill for 10 minutes and drying in an oven at 60°C. The dried material was then gently disaggregated using an agate pestle and mortar. Subsequent XRD analysis showed the presence of quartz, plagioclase, K-feldspar, muscovite/illite and chlorite in all samples, sometimes with additional calcite (LVF1 and LVF34) or kaolinite (LVF4 and LVF22) (Table 1). The total phyllosilicate content varied between 20% (LVF34) and 57% (LVF21).

3.1.2 Experimental apparatus and procedure

Friction experiments were performed using a triaxial deformation apparatus, described in detail by Mitchell and Faulkner (2008) and Faulkner and Armitage (2013). In this apparatus, the sample is located between two grooved, L-shaped sliders that allow fluid access into the sample via porous plates (Sánchez-Roa et al., 2016). Servo-controlled fluid systems control the confining and pore fluid pressure, while axial loading occurs via a servo-controlled gear train. The sample assembly plus vessel are externally heated, via three external furnaces, controlled

within 0.1°C. The axial load cell located at the bottom of the vessel is water-cooled to reduce thermal drift.

Samples of 20 x 36 mm were prepared by pre-pressing 1.2 grams of dry powder on one of the sliders at ~5 MPa for several seconds at room temperature, yielding a thickness of just over 1 mm. Silicon rubber fillers were used to accommodate the displacement via shear of the sample. The sample-slider combination was wrapped in a thin sheet of PTFE to allow easy insertion in the jacket, consisting of PVC for the room temperature experiments and Viton rubber for the experiments at elevated temperature. A thin disk of PTFE was inserted at the top of the jacketed sample-slider set to allow for small lateral displacements of the sliders during any gouge layer compaction.

3.1.3 Experimental conditions

Shear experiments were performed at a confining pressure of 100 MPa and pore fluid pressure of 40 MPa, i.e. an effective normal stress of 60 MPa, at room temperature, 120°C and 170°C. The pressure conditions represent a depth of approximately 3.8 km, assuming a hydrostatic fluid pressure. The temperatures of 120°C and 170°C represent depths of about 5.0 and 6.4 km, respectively, based on the thermokinematic model by Simoes et al. (2007; see also Thomas et al., 2017). Although our experimental conditions correspond to depths shallower than those associated with seismicity on the LVF (e.g. Thomas et al., 2017), the range of temperatures considered here allow exploration of trends with temperature/depth and are thus likely to provide insight relevant for a large portion of the LVF.

During pressurizing and depressurizing of the setup, care was taken to maintain the effective normal stress below 60 MPa. The experiments at elevated temperature were left to equilibrate overnight. After a run-in of 2.5 mm at 0.3 µm/s, we applied velocity steps of 3 and 0.3 µm/s, each for 0.75 mm, yielding a total displacement of 6.25 mm. The slow run-in velocity was chosen to avoid any pore pressure effects due to shear-enhanced compaction (Faulkner et al., 2018). Load point displacement (resolution ± ~0.5 µm), confining pressure (± 0.01 MPa), pore fluid pressure (± 0.01 MPa), axial load (± 0.05 kN) and temperature (± 0.1°C) were measured and the corresponding signals logged at a frequency of 2 Hz.

3.1.4 Data processing

Axial load was converted to shear stress τ, which was subsequently used to determine the apparent coefficient of friction via $\mu = \tau / \sigma_{eff}$, where σ_{eff} is the effective normal stress defined as the difference between the normal stress σ and the pore fluid pressure P_f, i.e. $\sigma_{eff} = \sigma - P_f$. Note that we ignore cohesion and, following Behnsen and Faulkner (2012), jacket strength. Comparison of the axial force output pre- and post-experiment, under unloaded conditions, indicated a small drift of the measurement over the duration of an experiment mostly likely due to minor laboratory temperature fluctuations. We corrected the data for this drift, assuming a linear drift of the force with displacement. We explored the effect of assuming a linear drift with time versus with displacement but found no significant difference. The velocity dependence of friction was interpreted using the rate and state dependent friction (RSF) theory (Dieterich, 1978; 1979; Ruina, 1983) with the empirical Dieterich type ("slowness") formulation:

$$\tau = \mu\sigma_{eff} = \left[\mu_0 + a\ln\left(\frac{V}{V_0}\right) + b\ln\left(\frac{V_0\theta}{d_c}\right)\right]\sigma_{eff} \quad \text{with} \quad \frac{d\theta}{dt} = 1 - \frac{V\theta}{d_c} \qquad (1)$$

(e.g. Marone, 1998). Here, θ is an internal state variable, a represents the magnitude of the instantaneous change in μ upon a step change in sliding velocity from a value V_0 to a value $V = eV_0$, b reflects the magnitude of the change in μ during subsequent evolution to a new steady state value over a critical sliding distance d_c, and μ_o is the friction coefficient measured at velocity V_0. At a constant slip velocity V, the state variable θ evolves to the steady state (ss) value:

$$\frac{d\theta}{dt} = 1 - \frac{V\theta}{d_c} = 0 \qquad \text{i.e.,} \qquad \theta_{ss}(V) = \frac{d_c}{V} \tag{2a}$$

Substituting equation (2a) into equation (1) and rearranging yields for the corresponding steady state shear stress τ_{ss}:

$$\tau_{ss} = \mu_{ss}\sigma_{eff} = \left[\mu_0 + (a-b)\ln\left(\frac{V}{V_0}\right)\right]\sigma_{eff} \tag{2b}$$

For changes in steady state friction coefficient ($\Delta\mu_{ss}$) resulting from a stepwise change in velocity, and keeping σ_{eff} constant, equation (1) yields:

$$\Delta\tau_{ss} = \Delta\mu_{ss}\sigma_{eff} = (a-b)\left[\ln\left(\frac{V_2}{V_0}\right) - \ln\left(\frac{V_1}{V_0}\right)\right]\sigma_{eff} \tag{3a}$$

$$\text{i.e., } (a-b) = \frac{\Delta\mu_{ss}}{\ln\left(\frac{V_2}{V_1}\right)} = \frac{\Delta\mu_{ss}}{\Delta\ln V} \tag{3b}$$

(e.g. Marone, 1998). Positive (a–b) values indicate an increase in steady state friction coefficient with increasing velocity, i.e. velocity-strengthening, which precludes nucleation of unstable slip, whereas negative (a-b) values signify velocity-weakening and the potential to nucleate unstable slip (e.g. Scholz, 1998). We used the non-linear least squares numerical fitting routine including apparatus stiffness developed by Noda and Shimamoto (2009) for fitting of the velocity steps to obtain separate values for a and b, and d_c (see also Sánchez-Roa et al., 2016).

3.2 Microstructural methods

The slider-sample setup was dried overnight at 80°C before taking the sliders apart and recovering the wafer of material, which often broke in multiple pieces. Oriented pieces were subsequently impregnated under vacuum and sections for microstructural investigation were prepared. An FEI Quanta FEG 650 Scanning Electron Microscope (SEM) with an Oxford Instruments X-max 150^N Energy Dispersive X-ray (EDX) detector was used to examine the polished sections. The SEM was operated at low vacuum (0.82 Torr) at 20kV, and the samples were analysed uncoated.

3.3 Geodetic methods

3.3.1 Kinematic analysis and determination of slip history

Using the dense set of geodetic, remote sensing and seismological data available, Thomas et al. (2014a) performed a kinematic analysis on the LVF. The study spans the period from 1992 to 2010, and applies the PCAIM technique (Kositsky & Avouac, 2010) to obtain timeseries of slip at depth with the same temporal resolution provided by the data, i.e., daily. The analysis encompassed the 2003 Chengkung earthquake, as well as the pre- and postseismic period. It was determined that, in the southern section of the LVF, a large fraction (80–90%) of slip is aseismic whereas the northern part is almost fully locked. This is illustrated by the interseismic coupling

(ISC) map displayed in Figure 1b. ISC quantifies the degree of locking of the fault: if ISC = 1, the fault patch is fully locked, if ISC = 0 the patch is creeping at the long-term slip rate. The latter was determined by using the Euler pole formalism to describe the long-term motion of the Coastal Range (CoR) and Central Range (CeR) block, which bound the Longitudinal Valley Fault to the east and west, respectively (Supporting Figure S1a). The coupling map shows in particular that creep was inferred at the surface along the southern portion of the LVF, where it seems to correlate with the occurrence of the Lichi mélange (Figure 1a). Thomas et al. (2014a) also found that the 2003 Chengkung earthquake occurred on a fault patch which had remained partially locked in the interseismic period. Moreover, the seismic rupture failed to reach the surface and afterslip occurred around the area that ruptured seismically. Figure S2, in the supplementary material, displays the pre-, co- and post-seismic inversion models used in this study and Figure S3 gives the corresponding resolution maps of these models.

3.3.2 Method to derive mechanical properties from geodetic observations

The inferred time series of slip at depth obtained from the kinematic analysis can further be used to derive some of the fault friction properties (e.g. Thomas et al., 2017). In Supporting Figure S4 we display the time series of 15 patches that are used later in this work to make a comparison with the laboratory-derived values (cf. Section 5.3).

To derive the frictional properties using the time series, we first assume that the LVF fault obeys a rate-and-state friction law with the aging form of the state variable evolution as defined in equation (1). Knowing the change in stress resulting, for example, from a nearby coseismic event, and knowing the slip velocity before and after the mainshock, one can derive the frictional parameter $(a\text{-}b)\sigma_{eff}$ for each creeping patch using equations (3):

$$(a-b)\sigma_{eff} = \frac{\Delta\tau_{ss}}{\Delta \ln V} \tag{4a}$$

However here, unlike for laboratory experiments, for which we have a control on the applied stresses, the earthquake might have induced a change in the effective normal stress. Therefore, following (e.g. Perfettini & Avouac, 2004; cf. equation (2)), we replace $\Delta\tau_{ss}$ by the the static Coulomb stress change (ΔCFF), leading to :

$$(a-b)\sigma_{eff} = \frac{\Delta \mathrm{CFF}}{\Delta \ln V} = \frac{\Delta\tau_{ss} - \mu_0 \Delta\sigma_{ss}}{\ln\left(\frac{V^+}{V_{int}}\right)} \tag{4b}$$

with the geomechanical convention that normal stress is positive in compression. However, as shown by Thomas et al. (2017; Figure 4), it is worth mentioning that $\mu_0\Delta\sigma_{ss}$ is significantly smaller than $\Delta\tau_{ss}$. Moreover, with this method, the implied assumption is that the fault has reached a steady state condition. It is a fair supposition since the data we used to infer $(a\text{-}b)\sigma_{eff}$ have a resolution of one day, which is not precise enough to sample the early increase of postseismic slip rate that reflects the adjustment of the state variable. Changes in shear stress induced by the main shock are inferred using the kinematic slip model of the 2003 Chengkung earthquake for a rake corresponding to the long-term motion of the fault . V_{int} is directly retrived form the secular interseismic model (see Figure S2a and Supplementary Text S1 and S2 for more details) and V^+ are then determined by fitting the timeseries of slip $U(t)$ at depth on each patch with the analytical solution derived by Perfettini and Avouac (2004):

$$U(t) \approx V_{int} t_r \ln\left(1 + \frac{V^+}{V_{int} t_r} t\right) \tag{5}$$

where t_r is the relaxation time. In this model, the elastic interactions between neighbouring creeping patches during postseismic motion are neglected. This method is by definition only applicable to patches displaying velocity-strengthening behaviour during the afterslip and for which a positive Coulomb stress change can be assumed. Note that, although (a-b) can be derived for lab-data in which σ_{eff} was imposed (equation (3b)), the absence of accurate information on variation of σ_{eff} with depth, along the LVF, means that we can only reliably extract the product of (a-b) and σ_{eff} from geodetic data.

4 Results

4.1 Mechanical data derived from laboratory experiments

A list of experimental conditions and key mechanical data is provided in Table 2.

Table 2. List of experiments, conditions and key data. P_c = confining pressure, P_f = pore fluid pressure, $V_{run\text{-}in}$ = starting slip velocity, before the onset of velocity-stepping, $D_{run\text{-}in}$ = displacement before the onset of velocity-stepping, V_{step} = slip velocity imposed during velocity-stepping, D_{step} = displacement during velocity-stepping, μ_{yield} = friction coefficient at the yield point, μ_{final} = final friction coefficient.

Experiment	**Sample**	P_c **(MPa)**	P_f **(MPa)**	T **(°C)**	$V_{run\text{-}in}$ **(µm/s)**	$D_{run\text{-}in}$ **(mm)**	V_{step} **(µm/s)**	D_{step} **(mm)**	μ_{yield}	μ_{final}
LVF1_RT	LVF1	100	40	22	0.3	2.5	3-0.3-3-0.3-3	0.75	0.46	0.47
LVF4_RT	LVF4	100	40	22	0.3	2.5	3-0.3-3-0.3-3	0.75	0.28	0.28
LVF21_RT	LVF21	100	40	22	0.3	2.5	3-0.3-3-0.3-3	0.75	0.44	0.44
LVF22_RT	LVF22	100	40	22	0.3	2.5	3-0.3-3-0.3-3	0.75	0.32	0.33
LVF34_RT	LVF34	100	40	22	0.3	2.5	3-0.3-3-0.3-3	0.75	0.51	0.56
LVF4_120C	LVF4	100	40	120	0.3	2.5	3-0.3-3-0.3-3	0.75	0.31	0.33
LVF34_120C	LVF34	100	40	120	0.3	2.5	3-0.3-3-0.3-3	0.75	0.55	0.64
LVF4_170C	LVF4	100	40	170	0.3	2.5	3-0.3-3-0.3-3	0.75	0.30	0.33
LVF21_170C	LVF21	100	40	170	0.3	2.5	3-0.3-3-0.3-3	0.75	0.50	0.55
LVF34_170C	LVF34	100	40	170	0.3	2.5	3-0.3-3-0.3-3	0.75	0.53	0.61
KAO_RT	KGa-1b	100	40	22	0.3	2.5	3-0.3-3-0.3-3	0.75	0.35	0.29
LVF21_KAO_RT	88:12 LVF21:KGa-1b	100	40	22	0.3	2.5	3-0.3-3-0.3-3	0.75	0.41	0.44

4.1.1 Mechanical properties of samples with different origins

Friction curves for samples from both the partially locked and creeping section at room temperature are shown in Figure 2a. For all samples, μ increases rapidly at the first ~0.5 mm of displacement, at which point apparent yielding occurs, at μ values of 0.44-0.51 for samples from the partially locked section versus 0.28-0.32 for the samples from the creeping section. Apparent yielding is followed by sliding at near steady state friction levels with superimposed small variations related to steps in the sliding velocity. The shape of the stress strain curve suggests that pore pressure transients did not develop within the gouge during loading to yield. None of the characteristic features, such as marked strain weakening followed by prolonged strain hardening, associated with the transients were seen in the recorded data (see Faulkner et al., 2018). All samples display velocity-strengthening behaviour, but only samples from the partially locked section show a clear peak friction value followed by a decay to a new steady state friction coefficient following a step in slip velocity (i.e. a well resolvable direct and evolution effect);

samples from the creeping section lack the peak in friction. Final friction coefficients reached are 0.44-0.56 and 0.28-0.33 for samples from the partially locked and creeping section.

The velocity-strengthening behaviour is quantified in Figure 3. At room temperature, values of a are smaller for samples from the creeping section than from the partially locked section (cf. Supporting Figure S5), varying between 0.0034 for sample LVF4 from the creeping section to 0.0102 for LVF34 from the partially locked section. Similarly, values of b are smaller for samples from the creeping section and larger for samples from the partially locked section, reaching a minimum of -0.0074 for LVF22 from the creeping section and a maximum value of 0.0076 for LVF34 from the partially locked section. The critical slip distance d_c shows somewhat more variability for samples from the different fault sections at room temperature, but generally larger values for samples from the creeping section (up to 145 μm for LVF22) than from the partially locked section (down to 4.54 μm for LVF34). Finally, (a-b) values at room temperature are all positive, supporting the velocity-strengthening behaviour inferred from Figure 2. The samples from the creeping section show more pronounced velocity-strengthening behaviour, reaching values as high as 0.0122 for LVF22, while the samples from the partially locked section show closer to neutral velocity-dependence, with values as low as 0.001 for LVF34.

4.1.2 Effect of temperature

The effect of temperature on the frictional behaviour of selected samples is shown in Figure 2b. Friction curves at 120°C and 170°C are very similar to those at room temperature, but reaching higher steady state μ values, up to 0.64 and 0.61 at 120°C and 170°C for samples from the partially locked section and up to 0.33 at both 120°C and 170°C for samples from the creeping section. As at room temperature, steps in the slip velocity result in small changes in the friction coefficient, showing a clear peak in the friction coefficient immediately after a velocity step only for the samples from the partially locked section. Velocity-dependence as a function of temperature is quantified in Figure 3.

Figure 3 shows slightly positive trends for a as a function of temperature, for both LVF4 from the creeping section and LVF34 from the partially locked section. Sample LVF21, on the other hand, which showed a spread of values at room temperature, shows on average slightly reduced a values at 170°C. Values of b tend to be similar at higher temperatures as at room temperature with a somewhat larger spread for LFV34. No trends can be observed for d_c as a function of temperature. In contrast, values of (a-b) show clear trends with temperature, where (a-b) values for LVF4 from the creeping zone become more positive with increasing temperature, while those for LVF34 from the partially locked zone decrease with temperature and become negative at 120°C and 170°C, which indicates velocity-weakening behaviour. Sample LVF21 shows only a minor decrease in (a-b) values and still shows velocity-strengthening behaviour at 170°C.

4.2 Microstructural observations

Figure 4a-e shows microstructures of the samples used in this study, all sheared at room temperature conditions. Both samples derived from the partially locked and creeping sections of the LVF show clasts of quartz and feldspar embedded in a clay matrix with little texture. Sample LVF1 (partially locked section; Figure 4a) contains clasts of up to about 100 μm in size and some indistinct P- and Y-shears (terminology after Logan et al., 1992). Sample LVF21 (partially locked section, Figure 4b) shows slightly smaller clasts (up to ~70 μm) and a larger fraction of

clay than LVF1, consistent with its composition (Table 1). Some of the clay in LVF21 is concentrated in clusters and P and R_1 Riedel shears can roughly be distinguished. Sample LVF34 (partially locked section, Figure 4c) is relatively rich in clasts, which reach sizes of just over 100 μm diameter, and does not show shear bands. The samples from the creeping section, LVF4 and LVF22 (Figure 4d and e) show relatively small clasts of up to several tens of μm and some weak P-, Y- and occasionally R_1 Riedel shears.

4.3 Mechanical data derived from geodetic observations

4.3.1 Mechanical properties of subsurface patches

To perform the slip inversion, the LVF was subdivided into 660 patches of 3.16 × 3.16 km. The displayed time-series are therefore an average of the slip happening over a ~10 km^2 area. Using the method described in Section 3.3, we derived the mechanical properties for all the patches displaying a positive coulomb stress change (Supporting Figure S1b) and postseismic slip rate greater than for the interseismic model (see Supporting Figure S2). For each patch the kinematic analysis provides the time evolution of slip along the direction of the slip vector predicted by the block motion of the Coastal Range relative to the Central Range (e.g., Supporting Figure S4). To derive the parameter $(a\text{-}b)\sigma_{eff}$, we computed the ΔCFF from the coseismic model derived by Thomas et al. (2014a), using the Coulomb3 software (Lin & Stein, 2004). We estimated the change in stress for a rake that corresponds to the direction of the slip vector predicted by the block motion of the Coastal Range relative to the Central Range, assuming a constant strike equal to the average fault strike of 23.4° (Supporting Figure S1b). We then fitted the time evolution of slip following equation (5) to get V^+. We finally applied equation (4b) to derive $(a\text{-}b)\sigma_{eff}$ (Supporting Figure S1c). We directly used the time-series inferred for each patch, and not some average over the neighbouring patches, because of the good resolution of the inversion models. Indeed, up-dip from the coastline, the resolution is generally smaller than 5 km (see Supporting Figure S3). Near the fault trace, the resolution is as good as 511 m for the interseismic model, 590 m for the coseismic model and 509 m for the postseismic model. As consequence, we consider that the slip happening over a ~10 km^2 area is well-resolved, and so are the inferred $(a\text{-}b)\sigma_{eff}$ values, for the patches on the west part of the coastline.

More specifically, the mechanical properties for the patches at the location of the five samples (square symbols) are displayed in Figure 5 and summarized in Supporting Table S1. Patches 526, 616 and 511, which correspond respectively to the Paliwan (LVF1, LVF21) and the Fanshuliao (LVF34) samples, show values ranging from ~0.01 to 0.08 MPa. Presuming σ_{eff} is known, the friction parameter $(a\text{-}b)$ can be determined. A common assumption is to calculate σ_{eff} for a given rock density, here 2700 kg/m^3, assuming a hydrostatic pore fluid pressure (Supporting Figure S6b). For the patches near the surface, this gives an average value of 27.1 MPa. Consequently, the inferred $(a\text{-}b)$ values for patches 526, 616 and 511 are very close to velocity neutral: 0.0003 to 0.0029 (Supporting Figure S7). These results are consistent with the high values of coupling (Figure 1c-d) inferred for those patches. On the other hand, patches 331 and 271 display values one order of magnitude higher. They sample the creeping zone and correspond to the Lichi mélange (samples LVF22 and LVF4). Both patches return a value of 0.4 MPa for the parameter $(a\text{-}b)\sigma_{eff}$ (Figure 5), which leads to $(a\text{-}b) = 0.0149$ (Supporting Figure S7), assuming hydrostatic pore pressure. Using our experimental data, a direct comparison with the frictional properties obtained from field-derived samples is now possible.

4.3.2 Effect of temperature

To infer the impact of temperature on the friction parameter $(a\text{-}b)\sigma_{eff}$, using the kinematic analysis, we assumed that the lithology varies little with depth and we used the patches in the vicinity of the collected samples. We explored two cases: we computed the friction parameters for the next two patches from that corresponding to the sample location following (i) a profile perpendicular to the fault (circle symbols in Figure 5), or (ii) following the slip vector predicted by the block motion of the Coastal Range relative to the Central Range (Supporting Figure S1a for the slip direction and diamond symbols in Figure 5). The exact location of these patches is given in Figure 1c-f. This choice is motivated by several reasons. First, the kinematic analysis of the LVF has demonstrated that the slip vector direction varies over the seismic cycle, showing a predominant dip-slip motion during the co-seismic periods and a predominant strike-slip motion over the pre- and post-seismic period (Thomas et al., 2014a). Secondly, the inferred direction of the long-term slip vector on the LVF is inevitably influenced by the lack of data on the hanging wall (at sea) and it should be taken with caution. By exploring these two cases we therefore encompass the possible range of values for a transpressive fault. The temperature corresponding to the depth of the considered patches is directly derived from the thermokinematic model of Simoes et al. (2007). The temperature-depth profile, for the center section of the LVF, is displayed in Supporting Figure S6c.

From north to south, the samples collected in the partially locked sections are LVF21, LVF1 and LVF34 respectively. For sample LVF21, based on geodesy, the inferred values of $(a\text{-}b)\sigma_{eff}$ at temperatures up to 189°C stay close to 0 MPa (0.0 to 0.03 MPa), which yields a maximum value of 0.0005 for $(a\text{-}b)$, i.e. velocity-neutral behaviour. Further south (sample LVF1), we observe two different trends depending on which slip profile we follow. Inferring the impact of temperature by following a profile perpendicular to the strike leads to an increase of $(a\text{-}b)\sigma_{eff}$ with temperature from 0.04 at 32°C to 0.39 MPa at 189°C (Figure 5, circle symbols), which leads to a maximum value of $(a\text{-}b) = 0.0043$. Whereas patch 512, that follows the long-term slip direction, stays close to velocity neutral, i.e. $(a\text{-}b)\sigma_{eff} = 0.09$ MPa and $(a\text{-}b) = 0.0014$. No values could be estimated for patch 498 which displays a postseismic slip rate lower than the preseismic. The discrepancy between these estimates can be explained by the fact that, based on the interseismic coupling map, patches 527 and 528 sample a creeping zone (ISC ≤ 0.11) whereas patch 512 corresponds to a partially locked zone (ISC = 0.45), like patch 526. Such a difference in coupling number could reflect a change in lithology, contradicting the initial assumption we made that the same material prevails when following a profile perpendicular to the fault. If this explanation is the most straightforward, it is important to underline that a higher ISC coupling could also reflect how close a patch is to a fully locked asperity of significant size (e.g. Bürgmann et al., 2005, Fig. 9), even though the patch samples a zones with velocity-strengthening frictional properties. In that case, the difference in the inferred $(a\text{-}b)\sigma_{eff}$ values between patches 527/528, and patch 512 could be related to the simple model we use, that ignores stress interaction between neighboring patches. Finally, for sample LVF34, only estimates for the along-dip profile could be computed, as the other patches displayed a postseismic slip rate lower than the preseismic. Patch 512 ($T = 94$°C) and patch 513 ($T = 189$°C) return a value of $(a\text{-}b)\sigma_{eff} = 0.09$ and 0.14 MPa respectively, which corresponds to $(a\text{-}b) = 0.0014$ and 0.0013 if we assume a hydrostatic pore pressure.

The patches corresponding to the two Lichi mélange samples displayed higher $(a\text{-}b)\sigma_{eff}$ values in general (Figure 5). For the patches in the vicinity of sample LVF4, we observe a slight

increase of $(a\text{-}b)\sigma_{eff}$ with temperature when we follow the along-dip profile, from 0.40 MPa at 32°C to 0.45 MPa at 94°C and 0.46 MPa at 189°C. This corresponds to the estimated values of 0.0419, 0.0069 and 0.0042 respectively for (a-b) (Supporting Figure S7). On the other hand, if we follow the long-term slip direction, the inferred $(a\text{-}b)\sigma_{eff}$ are significantly higher: 1.63 MPa at 94°C and 1.04 MPa at 189°C. The corresponding (a-b) values are 0.0247 and 0.0095. The second Lichi mélange sample, LVF22, was collected within an area which is more heterogeneous in terms of slip behaviour (see interseismic coupling map in Figure 1b). Following the along-dip profile, patch 272 (T = 94°C) and patch 273 (T = 189°C) return $(a\text{-}b)\sigma_{eff}$ values of 0.91 and 0.41 MPa respectively, which translate to (a-b) values of 0.0138 and 0.0038. For the profile following the slip vector, the inferred friction parameters are close to the value inferred near the surface, i.e. 0.46 MPa for patch 257 (T = 94°C) and 0.30 MPa for patch 243 (T = 189°C). The corresponding (a-b) values are 0.0070 and 0.0027 respectively. Thus, an increase of the friction parameter $(a\text{-}b)\sigma_{eff}$ with temperature (Figure 5), as for the patches relevant for LVF4, is followed by near velocity-neutral behaviour at 189°C. Since the patches 243 and 273 are adjacent to the partially locked section that ruptured during the 2003 Chengkung earthquake, this might reflect a change in lithology rather than the impact of increasing temperature.

5 Discussion

5.1 Comparison between samples from the partially locked versus creeping section

Our friction experiments on samples from the LVF show a remarkable difference in the behaviour of samples derived from the partially locked versus the creeping sections. Particularly, the samples from the creeping section (LVF4 and LVF22) are noticeably weaker than those from the partially locked section (LVF1, LVF21 and LVF34) with friction coefficients on average being 0.19 lower for the former (Figure 2, Table 2). In addition, the velocity-dependent response of samples from the two different locations is different, with only the samples from the partially locked section showing clear peaks in friction upon a step-change in the slip velocity (Supporting Figure S5). Samples from the creeping section do not show such a peak, which is quantified by negative b values (Figure 3). Furthermore, with increasing temperature, the RSF response of samples from the creeping versus partially locked section differs, with an increase in the magnitude of velocity-strengthening behaviour for the sample from the creeping section, as opposed to a decrease in the magnitude of velocity-strengthening behaviour or even the onset of velocity-weakening behaviour with increasing temperature for the samples from the partially locked section. This is consistent with the findings by Ikari et al. (2011) that weak gouges, with coefficients of friction μ <0.5, exhibit predominantly stable sliding behaviour, whereas strong gouges, with $\mu \geq 0.5$, exhibit both stable and unstable slip.

5.2 Deformation mechanisms for samples from partially locked versus creeping sections

Inspection of Table 1 suggests that the different frictional behaviour of samples from the creeping versus the partially locked section may be related to the composition of the two groups of samples. Notably, both samples from the creeping section (LVF4 and LVF22) contain 11-12% of kaolinite, while none of the samples from the partially locked section (LVF1, LVF21 and LVF34) contain kaolinite. We investigated the effect of kaolinite on the frictional behaviour of LVF via the additional experiments shown in Figures 6. Particularly, we added 12 wt% of kaolinite to sample LVF21, which was the sample from the partially locked section that was

otherwise most similar in composition to those from the creeping section (calcite is present in all these samples).

Figure 6 shows curves of the friction coefficient versus load point displacement for LVF21, which does not contain natural kaolinite, LVF22, which naturally contains 12% kaolinite, and, as comparison, LVF21 to which 12 wt% of kaolinite is added (88:12 LVF21:KAO), as well as near-pure kaolinite. The addition of kaolinite to LVF21 slightly reduces the friction coefficient at load point displacements up to about 4 mm, after which the friction coefficients of LVF21 with and without added kaolinite become indistinguishable. The friction coefficient of 88:12 LVF21:KAO is 0.13 higher than that of LVF22 at all displacements. The friction coefficient of near-pure kaolinite shows, in contrast to the curves for the LVF samples, a clear peak around the yield point, followed by a drop in the friction coefficient to values just below 0.3, which is only 0.03-0.04 lower than the friction coefficient for LVF22. Both 88:12 LVF21:KAO and near-pure kaolinite show a minor peak in the friction coefficient upon a step-change in slip velocity, which is distinctly different from LVF22 and somewhat similar to LVF21. Supporting Figure S8 shows the RSF parameters of the same sample set as was plotted in Figure 6, as a function of the kaolinite content. Though the data are limited, no trends in the RSF parameters with the kaolinite content can be observed. Notably, LVF21, 88:12 LVF21:KAO and near-pure kaolinite all have very similar a, b and (a-b) values. This is in contrast to LVF22, which has smaller a and b values and larger (a-b) values than all the other samples (Supporting Figure S8). Values of d_c take a wide range, with the largest values being attained by LVF22.

Based on the data shown in Figure 6 and Supporting Figure S8 we infer that the addition of kaolinite to LVF21 does not significantly change its frictional behaviour. Thus, the addition of kaolinite to the sample from the partially locked section does not change its behaviour to become similar to that of samples from the creeping section. We therefore investigated the microstructure of the sample with artificially added kaolinite, 88:12 LVF21:KAO, shown in Figure 4f, and compared it with that of the natural samples. The microstructure of 88:12 LVF21:KAO is very similar to that of the natural samples (both from the partially locked and creeping sections) in that it does not show a clear texture; only some indistinct shear bands can be seen. A notable difference of the microstructure of 88:12 LVF21:KAO compared to LVF22 and LVF4 is that the kaolinite that was added in 88:12 LVF21:KAO, is present in clusters (Figure 4f; Supporting Figures S9 and S10). Such clusters of kaolinite were not observed in the compositionally equivalent sample to 88:12 LVF21:KAO, i.e. LVF22. No kaolinite could be distinguished in LVF22, suggesting that it is present as dispersed, fine grains. This observation has two implications. Firstly, it shows that a difference in the distribution of kaolinite in compositionally equivalent gouges can result in distinctly different frictional behaviour (cf. 88:12 LVF21:KAO and LVF22 in Figure 6). Secondly, it suggests that a possible explanation for the frictional behaviour of LVF materials, both in the lab and in nature, may be the presence and distribution of kaolinite. This is consistent with previous studies in which clay minerals were inferred to control fault behaviour (e.g. Collettini et al., 2009; Lockner et al., 2011; Moore & Rymer, 2007). Finally, note that Wu et al. (2020) recently suggested that the observed creeping behaviour of the LVF at shallow depths may be related to gouge amorphization. Our data does not allow for identification of possible amorphous material.

548 5.3 Relationship between geodetic and laboratory data

549 To make a direct comparison between the experimental dataset and the results from the
550 kinematic inversion, we plotted the laboratory values (a-b) times the effective normal stress on
551 Figure 5 (triangle symbols). As described in Section 3.1, shear experiments were performed at an
552 effective normal stress of 60 MPa. Since we do not have a direct measurement of the effective
553 stress distribution along the LVF, this comparison is more robust than plotting the laboratory (a-
554 b) values against the (a-b) values derived from geodesy and an assumed effective normal stress
555 profile. Such a comparison can nevertheless be found in Supporting Figure S7 for completeness.
556 We note that our comparison does not account for any possible variations of the fault frictional
557 properties or interseismic slip rate with time. We have also not taken into account any possible
558 effects of pore fluid pressure transients following seismic slip on the effective normal stress.
559 Furthermore, we note that all our experiments were performed at a pore fluid pressure of 40
560 MPa, approximating to hydrostatic conditions, while pore fluid pressures in reality may divert
561 from hydrostatic. Den Hartog and Spiers (2013) measured a relatively small effect of pore fluid
562 pressure on frictional strength and stability of clay-rich gouges, suggesting that our comparison
563 may still be relevant for different pore fluid pressure conditions.

564 The primary point to emphasize is that, despite the fact that patches used for our
565 kinematic inversion represent the average behaviour of a 10 km^2 area, laboratory experiments
566 and inferences from the kinematic analysis are in very good agreement. Indeed, laboratory
567 experiment values of $(a\text{-}b)\sigma_{eff}$ vary from -0.28 to 0.73 MPa. If we compare the mean value
568 obtained from the experiments and the values derived from the patches at the location of the
569 samples, the difference is less than 13%. For example, the mean laboratory value for sample
570 LVF21 is 0.12 MPa, the corresponding inference for patch 616 is 0.08 (12% difference). Values
571 are summarized in Supporting Table S2 and displayed in Figure 5.

572 We next compare the trend with temperature for sample LVF21 and sample LVF34, from
573 the partially locked sections, and sample LVF4 from the creeping zone. Based on the laboratory
574 data, sample LVF21 from the Paliwan Formation displays a slight decrease in $(a\text{-}b)\sigma_{eff}$, from 0.20
575 MPa (T = 22°C) to 0.12 MPa (T = 170 °C), if we take the average. We observe a similar trend for
576 the values inferred from geodesy. Differences between the two datasets are less than 13% if we
577 compare the results at similar temperature. Note that velocity-neutral values are not necessarily
578 inconsistent with high value of coupling (Figure 1b). Materials displaying such behavior are very
579 sensitive to change in stresses and can appear both, in geodesy, as creeping or locked patches,
580 depending on how close they are to locked asperity. The Fanshuliao sample LVF34 also displays
581 a negative trend but $(a\text{-}b)\sigma_{eff}$ becomes negative at 120 and 170°C for the experiments. On the
582 other hand, values derived from the kinematic inversion show a slight increase in $(a\text{-}b)\sigma_{eff}$, and
583 because of the applied method, they are necessarily positive. Nevertheless, they stay close to
584 zero. Finally, the Lichi mélange sample LVF4 displays higher experimentally derived values that
585 increase with increasing temperature (from 0.39 MPa to 0.55 MPa). The values inferred from
586 geodesy, following the along-dip profile (circle symbols in Figure 5), are in very good agreement
587 (same trend, difference ≤ 10%). On the contrary, the values derived following the long-term slip
588 vector are in complete disagreement with the laboratory data (no trend, up to 107% difference).
589 The most likely explanation for this discrepancy is a variation of lithology with depth, which was
590 not accounted for in the kinematic inversion.

591 Overall, the two datasets agree remarkably well despite the different scale at which the
592 friction parameters were inferred (from 20 mm to 10 km^2) and the coarse thermokinematic model

used to infer the temperature at depth (Supporting Figure S6). First, and probably the most important point, is that the comparison supports the upscaling between laboratory experiments and numerical modelling of fault slip. Indeed, and rightfully so, the use of laboratory derived friction parameters, defined at a millimeter scale, to infer fault displacement (and sometimes hazard assessment) at hundreds of kilometre scale, has always been a matter of debate. Moreover, the similarity between the results underline the high potential of such a comprehensive approach in assessing hazard. A careful sampling campaign combined with a geodetic analysis of an active fault would allow for the development of predictive models of fault slip that include laboratory-derived frictional values at near-in situ conditions from the collected samples. This in turn could help to overcome the poor temporal resolution of geophysical data.

6 Conclusions

In this work we compared laboratory-determined frictional parameters of surface-derived samples from along the length of the LVF in Taiwan with the observed slip behaviour and with frictional parameters obtained geodetically. We performed shear experiments at an effective normal stress of 60 MPa, at room temperature, 120°C and 170°C and at slip velocities of 0.3-3 μm/s on 3 samples from the partially locked section and 2 samples from the creeping section of the LVF. In addition, timeseries of slip at depth along the LVF previously derived by Thomas et al. (2014a) from geodetic, remote sensing and seismological data were used to determine $(a\text{-}b)\sigma_{eff}$ at the patches corresponding to our sample locations. Our conclusions are as follows:

1. At room temperature, the frictional behaviour of samples from the partially locked versus creeping section of the LVF is distinctly different, with the former showing higher friction coefficients, larger values of a and b and smaller but still positive values of $(a\text{-}b)$.
2. At 120°C and 170°C, friction coefficients are higher than at room temperature, for both samples from the partially locked and creeping sections. Values of $(a\text{-}b)$ become more positive with increasing temperature for sample LVF4 from the creeping zone, whereas they become less positive for samples from the creeping zone (LVF34 and LVF21), reaching negative values at 120°C and 170°C for LVF34.
3. The microstructures of the samples after the shear experiments show little difference between the samples from the partially locked versus the creeping section, displaying clasts of quartz and feldspar embedded in a clay matrix with little texture.
4. At room/surface temperature, geodetically derived values of $(a\text{-}b)\sigma_{eff}$ derived for the patches corresponding to the location of the samples used for the experiments are an order of magnitude higher for the patches corresponding to the creeping zone than those for patches corresponding to the partially locked zone. At increased temperature, the values of $(a\text{-}b)\sigma_{eff}$ of patches corresponding to the creeping section are in general higher than those for patches corresponding to the partially locked section and dependent on the slip profile selected (perpendicular to the fault or following the long-term slip vector).
5. Addition of 12 wt% of kaolinite to LVF21 from the partially locked section to make it compositionally equivalent to LVF22 from the creeping section, did not significantly

change its frictional behaviour. Microstructural observations suggest that the presence and distribution of kaolinite may affect the frictional behaviour.

6. Overall, the frictional parameters derived from the experiments and those from modelling the geodetic observations of postseismic slip transients are in remarkable agreement, which supports the commonly used upscaling between laboratory experiments and numerical modelling of fault slip.

Acknowledgments, Samples, and Data

We thank J. Utley for his assistance with material preparation and for performing the XRD analysis, G. Coughlan for technical support for the experimental work and J. Buckman for performing the SEM analyses. R. Bürgmann and and anonymous reviewer are thanked for their constructive comments. No conflicts of interest exist that may have effected the results of this paper. The experimental data files are stored at Mendeley Data as den Hartog, S. A. M.; Thomas, M. Y.; Faulkner, D. R. (2021), "Laboratory-derived friction data for samples from the Longitudinal Valley Fault, Taiwan", Mendeley Data, v1; http://dx.doi.org/10.17632/dzcw4f9b9f.1. This project has received funding from the European Union's Horizon 2020 research and innovation programme under the Marie Sklodowska-Curie grant agreement No 658464. DRF acknowledges support from UK Natural Environment Research Council grant NE/P002943/1. This study was supported by the Agence National de la Recherche (ANR) IDEAS contract ANR-19- CE31-0004-01.

References

Angelier, J., Chu, H. T., & Lee, J. C. (1997). Shear concentration in a collision zone: kinematics of the Chihshang Fault as revealed by outcrop-scale quantification of active faulting, Longitudinal Valley, eastern Taiwan, *Tectonophysics*, *274*(1), 117-143, doi:https://doi.org/10.1016/S0040-1951(96)00301-0

Behnsen, J., & Faulkner, D. R. (2012). The effect of mineralogy and effective normal stress on frictional strength of sheet silicates, *Journal of Structural Geology*, *42*, 49-61,

Bürgmann, R. (2018). The geophysics, geology and mechanics of slow fault slip, *Earth and Planetary Science Letters*, *495*, 112-134, doi:https://doi.org/10.1016/j.epsl.2018.04.062

Bürgmann, R., Kogan, M. G., Steblow, G. M., Hilley, G., Levin, V. E., & Apel, E. (2005). Interseismic coupling and asperity distribution along the Kamchatka subduction zone, *Journal of Geophysical Research*, *110*, B07405, doi:10.1029/2005JB003648

Bürgmann, R., Schmidt, D., Nadeau, R. M., d'Alessio, M., Fielding, E., Manaker, D., McEvilly, T. V., & Murray, M. H. (2000). Earthquake Potential Along the Northern Hayward Fault, California, *Science*, *289*(5482), 1178-1182, doi:10.1126/science.289.5482.1178

Champenois, J., Fruneau, B., Pathier, E., Deffontaines, B., Lin, K. C., & Hu, J. C. (2012). Monitoring of active tectonic deformations in the Longitudinal Valley (Eastern Taiwan) using Persistent Scatterer InSAR method with ALOS PALSAR data, *Earth and Planetary Science Letters*, *337-338*, 144-155, doi:https://doi.org/10.1016/j.epsl.2012.05.025

Chen, H. Y., Lee, J. C., Tung, H., Yu, S. B., Hsu, Y. J., & Lee, H. (2012). Determination of vertical velocity field of southernmost longitudinal valley in eastern taiwan: A joint analysis of leveling and gps measurements, *Terrestrial Atmospheric and Oceanic Sciences*, *23*(4), 355-376,

Chlieh, M., Avouac, J. P., Sieh, K., Natawidjaja, D. H., & Galetzka, J. (2008). Heterogeneous coupling of the Sumatran megathrust constrained by geodetic and paleogeodetic measurements, *Journal of Geophysical Research: Solid Earth*, *113*(B5), doi:https://doi.org/10.1029/2007JB004981

Chung, L.-H., Chen, Y.-G., Wu, Y.-M., Shyu, J. B. H., Kuo, Y.-T., & Lin, Y.-N. N. (2008). Seismogenic faults along the major suture of the plate boundary deduced by dislocation modeling of coseismic displacements of the 1951 M7.3 Hualien–Taitung earthquake sequence in eastern Taiwan, *Earth and Planetary Science Letters*, *269*(3), 416-426, doi:https://doi.org/10.1016/j.epsl.2008.02.035

Collettini, C., Niemeijer, A., Viti, C., & Marone, C. (2009). Fault zone fabric and fault weakness, *Nature*, *462*(7275), 907-910, doi:10.1038/nature08585

Cross, R. S., & Freymueller, J. T. (2007). Plate coupling variation and block translation in the Andreanof segment of the Aleutian arc determined by subduction zone modeling using GPS data, *Geophysical Research Letters*, *34*(6), doi:https://doi.org/10.1029/2006GL028970

Den Hartog, S. A. M., Niemeijer, A. R., & Spiers, C. J. (2013). Friction on subduction megathrust faults: beyond the illite-muscovite transition, *Earth and Planetary Science Letters*, *373*, 8-19, doi:10.1016/j.epsl.2013.04.036

Den Hartog, S. A. M., Peach, C. J., De Winter, D. A. M., Spiers, C. J., & Shimamoto, T. (2012). Frictional properties of megathrust fault gouges at low sliding velocities: new data on effects of normal stress and temperature, *Journal of Structural Geology*, *38*, 156-171, doi:10.1016/j.jsg.2011.12.001

Den Hartog, S. A. M., & Spiers, C. J. (2013). Influence of subduction zone conditions and gouge composition on frictional slip stability of megathrust faults, *Tectonophysics*, *600*, 75-90, doi:10.1016/j.tecto.2012.11.006

Dieterich, J. H. (1978). Time-dependent friction and the mechanics of stick-slip, *Pure and Applied Geophysics*, *116*, 790-806,

Dieterich, J. H. (1979). Modeling of rock friction 1. Experimental results and constitutive equations, *Journal of Geophysical Research*, *84*(B5), 2161-2168,

Dublanchet, P., Bernard, P., & Favreau, P. (2013). Interactions and triggering in a 3-D rate-and-state asperity model, *Journal of Geophysical Research: Solid Earth*, *118*(5), 2225-2245, doi:https://doi.org/10.1002/jgrb.50187

Faulkner, D. R., & Armitage, P. J. (2013). The effect of tectonic environment on permeability development around faults and in the brittle crust, *Earth and Planetary Science Letters*, *375*(0), 71-77, doi:http://dx.doi.org/10.1016/j.epsl.2013.05.006

Faulkner, D. R., Lewis, A. C., & Rutter, E. H. (2003). On the internal structure and mechanics of large strike-slip fault zones: field observations of the Carboneras fault in southeastern Spain, *Tectonophysics*, *367*(3), 235-251, doi:https://doi.org/10.1016/S0040-1951(03)00134-3

Faulkner, D. R., Sanchez-Roa, C., Boulton, C., & den Hartog, S. A. M. (2018). Pore Fluid Pressure Development in Compacting Fault Gouge in Theory, Experiments, and Nature, *Journal of Geophysical Research: Solid Earth*, *123*(1), 226-241, doi:10.1002/2017jb015130

Hillers, G., & Wesnousky, S. G. (2008). Scaling Relations of Strike-Slip Earthquakes with Different Slip-Rate-Dependent Properties at Depth, *Bulletin of the Seismological Society of America*, *98*(3), 1085-1101, doi:10.1785/0120070200

723 Huang, C.-Y., Yuan, P. B., & Tsao, S.-J. (2006). Temporal and spatial records of active arc-
724 continent collision in Taiwan: A synthesis, *GSA Bulletin*, *118*(3-4), 274-288,
725 doi:10.1130/b25527.1
726 Hyndman, R. D., Yamano, M., & Oleskevich, D. A. (1997). The seismogenic zone of subduction
727 thrust faults, *The Island Arc*, *6*(3), 244-260, doi:10.1111/j.1440-1738.1997.tb00175.x
728 Ikari, M. J., Marone, C., & Saffer, D. M. (2011). On the relation between fault strength and
729 frictional stability, *Geology*, *39*(1), 83-86, doi:10.1130/G31416.1
730 Johnson, K. M., Bürgmann, R., & Larson, K. (2006). Frictional Properties on the San Andreas
731 Fault near Parkfield, California, Inferred from Models of Afterslip following the 2004
732 Earthquake, *Bulletin of the Seismological Society of America*, *96*(4B), S321-S338,
733 doi:10.1785/0120050808
734 Jolivet, R., Lasserre, C., Doin, M.-P., Guillaso, S., Peltzer, G., Dailu, R., Sun, J., Shen, Z.-K., &
735 Xu, X. (2012). Shallow creep on the Haiyuan Fault (Gansu, China) revealed by SAR
736 Interferometry, *Journal of Geophysical Research: Solid Earth*, *117*(B6),
737 doi:https://doi.org/10.1029/2011JB008732
738 Kositsky, A. P., & Avouac, J.-P. (2010). Inverting geodetic time series with a principal
739 component analysis-based inversion method, *Journal of Geophysical Research: Solid*
740 *Earth*, *115*(B3), doi:https://doi.org/10.1029/2009JB006535
741 Lee, J.-C., Angelier, J., Chu, H.-T., Hu, J.-C., & Jeng, F.-S. (2005). Monitoring active fault creep
742 as a tool in seismic hazard mitigation. Insights from creepmeter study at Chihshang,
743 Taiwan, *Comptes Rendus Geoscience*, *337*(13), 1200-1207,
744 doi:https://doi.org/10.1016/j.crte.2005.04.018
745 Lee, J.-C., Angelier, J., Chu, H.-T., Yu, S.-B., & Hu, J.-C. (1998). Plate-boundary strain
746 partitioning along the sinistral collision suture of the Philippine and Eurasian plates:
747 Analysis of geodetic data and geological observation in southeastern Taiwan, *Tectonics*,
748 *17*(6), 859-871, doi:10.1029/98tc02205
749 Lin, J., & Stein, R. S. (2004). Stress triggering in thrust and subduction earthquakes and stress
750 interaction between the southern San Andreas and nearby thrust and strike-slip faults,
751 *Journal of Geophysical Research: Solid Earth*, *109*(B2),
752 doi:https://doi.org/10.1029/2003JB002607
753 Liu, T. K., Chen, Y. G., Chen, W. S., & Jiang, S. H. (2000). Rates of cooling and denudation of
754 the Early Penglai Orogeny, Taiwan, as assessed by fission-track constraints,
755 *Tectonophysics*, *320*(1), 69-82, doi:https://doi.org/10.1016/S0040-1951(00)00028-7
756 Lockner, D. A., Morrow, C., Moore, D., & Hickman, S. (2011). Low strength of deep San
757 Andreas fault gouge from SAFOD core, *Nature*, *472*(7341), 82-85,
758 doi:10.1038/nature09927
759 Logan, J. M., Dengo, C. A., Higgs, N. G., & Wang, Z. Z. (1992). Fabrics of experimental fault
760 zones: their development and relationship to mechanical behavior, in *Fault Mechanics*
761 *and Transport Properties of Rocks*, edited by B. Evans, T.-F. Wong and W. F. Brace, pp.
762 33-67, Academic Press, London, doi:10.1016/S0074-6142(08)62814-4
763 Métois, M., Socquet, A., & Vigny, C. (2012). Interseismic coupling, segmentation and
764 mechanical behavior of the central Chile subduction zone, *Journal of Geophysical*
765 *Research: Solid Earth*, *117*(B3), doi:https://doi.org/10.1029/2011JB008736
766 Mitchell, T. M., & Faulkner, D. R. (2008). Experimental measurements of permeability
767 evolution during triaxial compression of initially intact crystalline rocks and implications

for fluid flow in fault zones, *Journal of Geophysical Research: Solid Earth*, *113*(B11), doi:doi:10.1029/2008JB005588

Moore, D. E., & Rymer, M. J. (2007). Talc-bearing serpentinite and the creeping section of the San Andreas fault, *Nature*, *448*(7155), 795-797, doi:http://www.nature.com/nature/journal/v448/n7155/suppinfo/nature06064_S1.html

Moore, J. C., Rowe, C. D., & Meneghini, F. (2007). How accretionary prisms elucidate seismogenesis in subduction zones, in *The Seismogenic Zone of Subduction Thrust Faults*, edited by T. H. Dixon and J. C. Moore, pp. 288-315, Columbia University Press, New York,

Murray, J. R., Segall, P., Cervelli, P., Prescott, W., & Svarc, J. (2001). Inversion of GPS data for spatially variable slip-rate on the San Andreas Fault near Parkfield, CA, *Geophysical Research Letters*, *28*(2), 359-362, doi:https://doi.org/10.1029/2000GL011933

Noda, H., & Shimamoto, T. (2009). Constitutive properties of clayey fault gouge from the Hanaore fault zone, southwest Japan, *Journal of Geophysical Research*, *114, B04409*, DOI:10.1029/2008JB005683, doi:10.1029/2008JB005683

Ozawa, S., Nishimura, T., Munekane, H., Suito, H., Kobayashi, T., Tobita, M., & Imakiire, T. (2012). Preceding, coseismic, and postseismic slips of the 2011 Tohoku earthquake, Japan, *Journal of Geophysical Research: Solid Earth*, *117*(B7), doi:https://doi.org/10.1029/2011JB009120

Perfettini, H., & Avouac, J.-P. (2004). Stress transfer and strain rate variations during the seismic cycle, *Journal of Geophysical Research: Solid Earth*, *109*(B6), doi:https://doi.org/10.1029/2003JB002917

Pritchard, M. E., & Simons, M. (2006). An aseismic slip pulse in northern Chile and along-strike variations in seismogenic behavior, *Journal of Geophysical Research: Solid Earth*, *111*(B8), doi:https://doi.org/10.1029/2006JB004258

Rousset, B., Jolivet, R., Simons, M., Lasserre, C., Riel, B., Milillo, P., Çakir, Z., & Renard, F. (2016). An aseismic slip transient on the North Anatolian Fault, *Geophysical Research Letters*, *43*(7), 3254-3262, doi:https://doi.org/10.1002/2016GL068250

Ruina, A. (1983). Slip instability and state variable friction laws, *Journal of Geophysical Research*, *88*(B12), 10359-10370,

Sánchez-Roa, C., Jiménez-Millán, J., Abad, I., Faulkner, D. R., Nieto, F., & García-Tortosa, F. J. (2016). Fibrous clay mineral authigenesis induced by fluid-rock interaction in the Galera fault zone (Betic Cordillera, SE Spain) and its influence on fault gouge frictional properties, *Applied Clay Science*, *134*, 275-288, doi:http://dx.doi.org/10.1016/j.clay.2016.06.023

Shyu, J. B. H., Chung, L.-H., Chen, Y.-G., Lee, J.-C., & Sieh, K. (2007). Re-evaluation of the surface ruptures of the November 1951 earthquake series in eastern Taiwan, and its neotectonic implications, *Journal of Asian Earth Sciences*, *31*(3), 317-331, doi:https://doi.org/10.1016/j.jseaes.2006.07.018

Shyu, J. B. H., Sieh, K., Avouac, J. P., Chen, W. S., & Chen, Y. G. (2006). Millennial slip rate of the Longitudinal Valley fault from river terraces: Implications for convergence across the active suture of eastern Taiwan, *Journal of Geophysical Research: Solid Earth (1978–2012)*, *111*(B8), doi:10.1029/2005JB003971

Simoes, M., Avouac, J. P., Beyssac, O., Goffé, B., Farley, K. A., & Chen, Y. G. (2007). Mountain building in Taiwan: A thermokinematic model, *Journal of Geophysical Research: Solid Earth (1978–2012)*, *112*(B11), doi:10.1029/2006JB004824

Suppe, J. (1984). Kinematics of arc-continent collision, flipping of subduction, and back-arc spreading near Taiwan, *Memoir. Geol. Soc. China*, *6*, 21-33,

Teng, L. S. (1981). Island arc system of the Coastal Range, eastern Taiwan, *Proc. Geol. Soc. China*, *24*, 99-112,

Teng, L. S., Chen, W. S., Wang, Y., Song, S.-R., & Lo, H.-J. (1988). Toward a comprehensive stratigraphic system of the coastal range, eastern Taiwan, *Acta Geologica Taiwanica*, *26*, 19-35,

Thomas, M. Y., Avouac, J.-P., Champenois, J., Lee, J.-C., & Kuo, L.-C. (2014a). Spatiotemporal evolution of seismic and aseismic slip on the Longitudinal Valley Fault, Taiwan, *Journal of Geophysical Research: Solid Earth*, *119*(6), 5114-5139, doi:10.1002/2013JB010603

Thomas, M. Y., Avouac, J.-P., Gratier, J.-P., & Lee, J.-C. (2014b). Lithological control on the deformation mechanism and the mode of fault slip on the Longitudinal Valley Fault, Taiwan, *Tectonophysics*, *632*, 48-63, doi:https://doi.org/10.1016/j.tecto.2014.05.038

Thomas, M. Y., Avouac, J.-P., & Lapusta, N. (2017). Rate-and-state friction properties of the Longitudinal Valley Fault from kinematic and dynamic modeling of seismic and aseismic slip, *Journal of Geophysical Research: Solid Earth*, *122*(4), 3115-3137, doi:https://doi.org/10.1002/2016JB013615

Titus, S. J., DeMets, C., & Tikoff, B. (2006). Thirty-Five-Year Creep Rates for the Creeping Segment of the San Andreas Fault and the Effects of the 2004 Parkfield Earthquake: Constraints from Alignment Arrays, Continuous Global Positioning System, and Creepmeters, *Bulletin of the Seismological Society of America*, *96*(4B), S250-S268, doi:10.1785/0120050811

Wallace, L. M., Beavan, J., McCaffrey, R., & Darby, D. (2004). Subduction zone coupling and tectonic block rotations in the North Island, New Zealand, *Journal of Geophysical Research: Solid Earth*, *109*(B12), doi:https://doi.org/10.1029/2004JB003241

Wang, Y., & Chen, W. (1993). Geological map of eastern coastal range, 1:100,000, Central Geological Survey, MOEA, Taiwan.

Wu, W.-J., Kuo, L.-W., Ku, C.-S., Chiang, C.-Y., Sheu, H.-S., Aprilniadi, T. D., & Dong, J.-J. (2020). Mixed-Mode Formation of Amorphous Materials in the Creeping Zone of the Chihshang Fault, Taiwan, and Implications for Deformation Style, *Journal of Geophysical Research: Solid Earth*, *125*(6), e2020JB019862, doi:https://doi.org/10.1029/2020JB019862

Wu, Y. M., Chen, Y. G., Shin, T. C., Kuochen, H., Hou, C. S., Hu, J. C., Chang, C. H., Wu, C. F., & Teng, T. L. (2006). Coseismic versus interseismic ground deformations, fault rupture inversion and segmentation revealed by 2003 Mw 6.8 Chengkung earthquake in eastern Taiwan, *Geophysical Research Letters*, *33*(2), doi:10.1029/2005gl024711

Yu, S.-B., & Kuo, L.-C. (2001). Present-day crustal motion along the Longitudinal Valley Fault, eastern Taiwan, *Tectonophysics*, *333*(1), 199-217, doi:https://doi.org/10.1016/S0040-1951(00)00275-4

Figure captions

Figure 1. (a) Geological map of eastern Taiwan (Thomas et al., 2014b), modified from Wang and Chen (1993). The Coastal Range is composed of three accreted Mio-Pliocene volcanic islands (Tuluanshan Formation), three remnants of Plio-Pleistocene forearc basins and intra-arc basins (Fanhsuliao, Paliwan and Shuilien conglomerate), and the Pliocene collision Lichi

mélange, which is related to the collision between the Luzon arc and the continental margin of South China. The Peinanshan and the Wuho are post-collision conglomerates. Central Range formations that border the Longitudinal Valley, include slates and schist. CF = Chimei Fault; LVF = Longitudinal Valley Fault; CeR = Central Range; CoR = Coastal Range. (b) Interseismic coupling (ISC) distribution (Thomas et al., 2014a) and location of the samples used in this study. The ISC quantifies the degrees of locking of the LVF fault (ISC = 1, the fault patch is fully locked, ISC = 0 the patch is creeping at the long-term slip rate, as defined in Supporting Figure S1a). Black star indicates the epicenter of the 2003 Chengkung earthquake (Chung et al., 2008). (c-f) Zoomed-in sections of the interseismic coupling map to display the location of the patches used to infer the frictional parameters on the fault, for this study.

Figure 2. Friction coefficient versus displacement for selected samples from the partially locked (indicated with "locked" in figure) and creeping zone (LVF1, LVF21 and LVF34 versus LVF4 and LVF22, respectively), at room temperature only (a) and elevated temperatures (b). The stepwise change in slip velocity is indicated by vertical ticks at the top of the diagrams.

Figure 3. Rate and state friction parameters versus temperature for the samples investigated here. (a) direct effect a, (b) evolution effect b, (c) critical sliding distance d_c and (d) slip stability parameter (a-b). Values for velocity steps with an increase in velocity are shown as upward pointing triangles, while values for velocity downsteps are shown as downward pointing triangles. Closed symbols represent second state variables (b and D_c).

Figure 4. Microstructures of samples sheared in this study. (a)-(c) are microstructures after experiments LVF1_RT (a), LVF21_RT (b) and LVF34_RT (c) performed on samples derived from the partially locked section (indicated with "locked" in the figure). (d) and (e) are microstructures after experiments LVF4_RT (d) and LVF22_RT (e) on samples derived from the creeping section. (f) is the microstructure after experiment LVF21_KAO_RT, performed on sample LVF21 from the partially locked section with added kaolinite to become compositionally similar to sample LVF22 from the creeping section (see Discussion). Shear sense is dextral in all micrographs as shown. Shear band nomenclature after Logan et al. (1992) and shown in (a).

Figure 5. Variation of the friction parameter $(a\text{-}b)\sigma_{eff}$ with temperature for laboratory-derived data (open triangle symbols) and inferred values using times series of slip at depth (solid symbols). For the latter, the corresponding temperature at the centre of the patches is based on the thermokinematic model of Simoes et al. (2007), as provided in Supporting Figure S6c. Colored square symbols correspond to the patches at the location of the samples used for experiments. For comparison, values inferred at the neighbouring patches are given (black squares). Colored circle and diamond symbols correspond to the patches following an along-dip and a long-term slip vector profile, respectively (see Figure 1c-f for location). Grey background emphasizes the samples collected within a high-rate creeping zone.

Figure 6. Friction coefficient versus displacement for samples with varying amounts of kaolinite: 0% for LVF21, 100% for pure kaolinite, 12% mixed kaolinite for 88:12 LVF21:KAO, and 12% natural kaolinite for LVF22_RT.

Figure1.

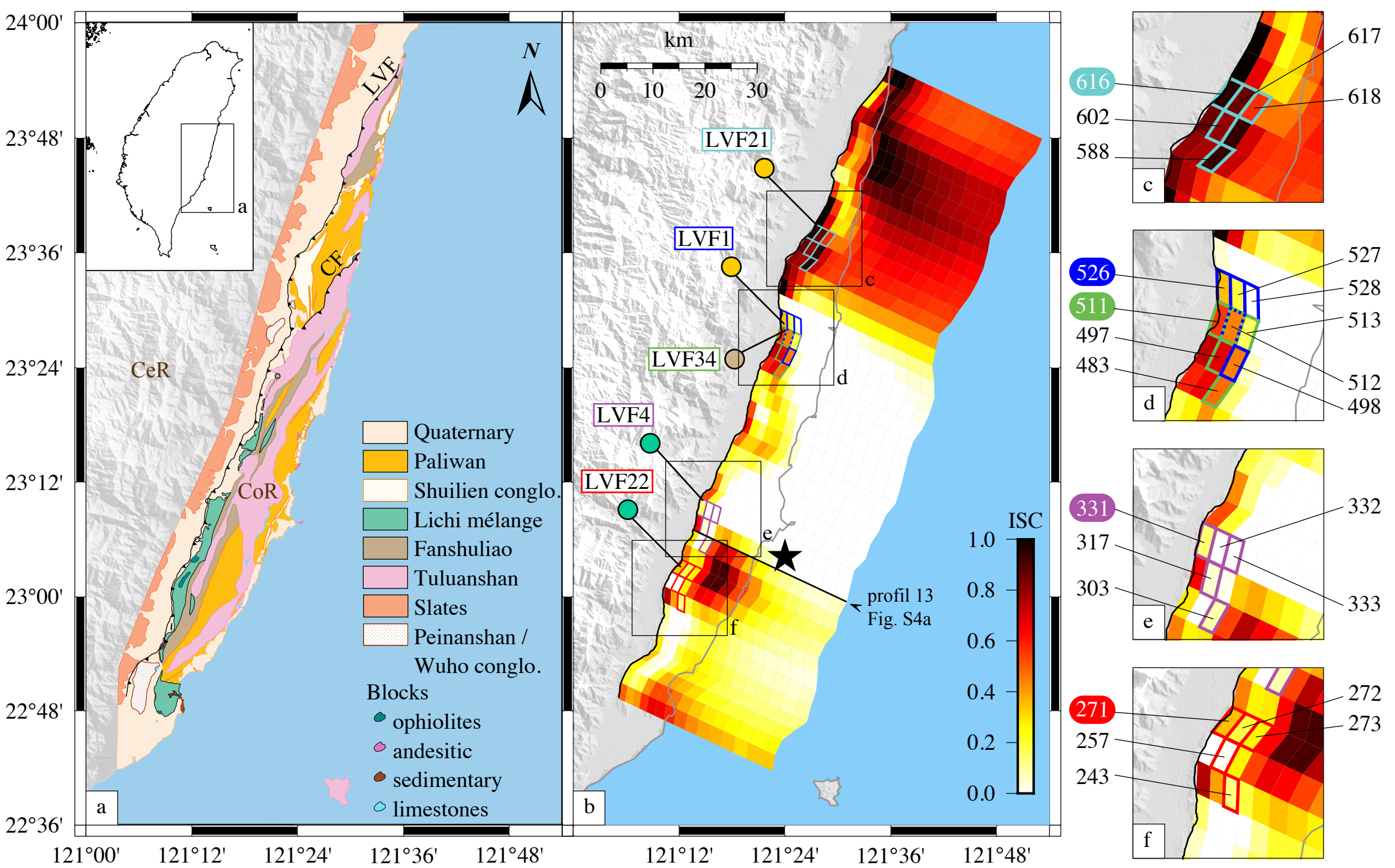
24°00'
23°48'
23°36'
23°24'
23°12'
23°00'
22°48'
22°36'
121°00'
121°12'
121°24'
121°36'
121°48'
N
LVF
CF
CeR
CoR
a
Quaternary
Paliwan
Shuilien conglo.
Lichi mélange
Fanshuliao
Tuluanshan
Slates
Peinanshan /
Wuho conglo.
Blocks
ophiolites
andesitic
sedimentary
limestones
km
0
10
20
30
LVF21
LVF1
LVF34
LVF4
LVF22
c
d
e
f
b
profil 13
Fig. S4a
ISC
1.0
0.8
0.6
0.4
0.2
0.0
616
602
588
617
618
c
526
511
497
483
527
528
513
512
498
d
331
317
303
332
333
e
271
257
243
272
273
f

Figure2.

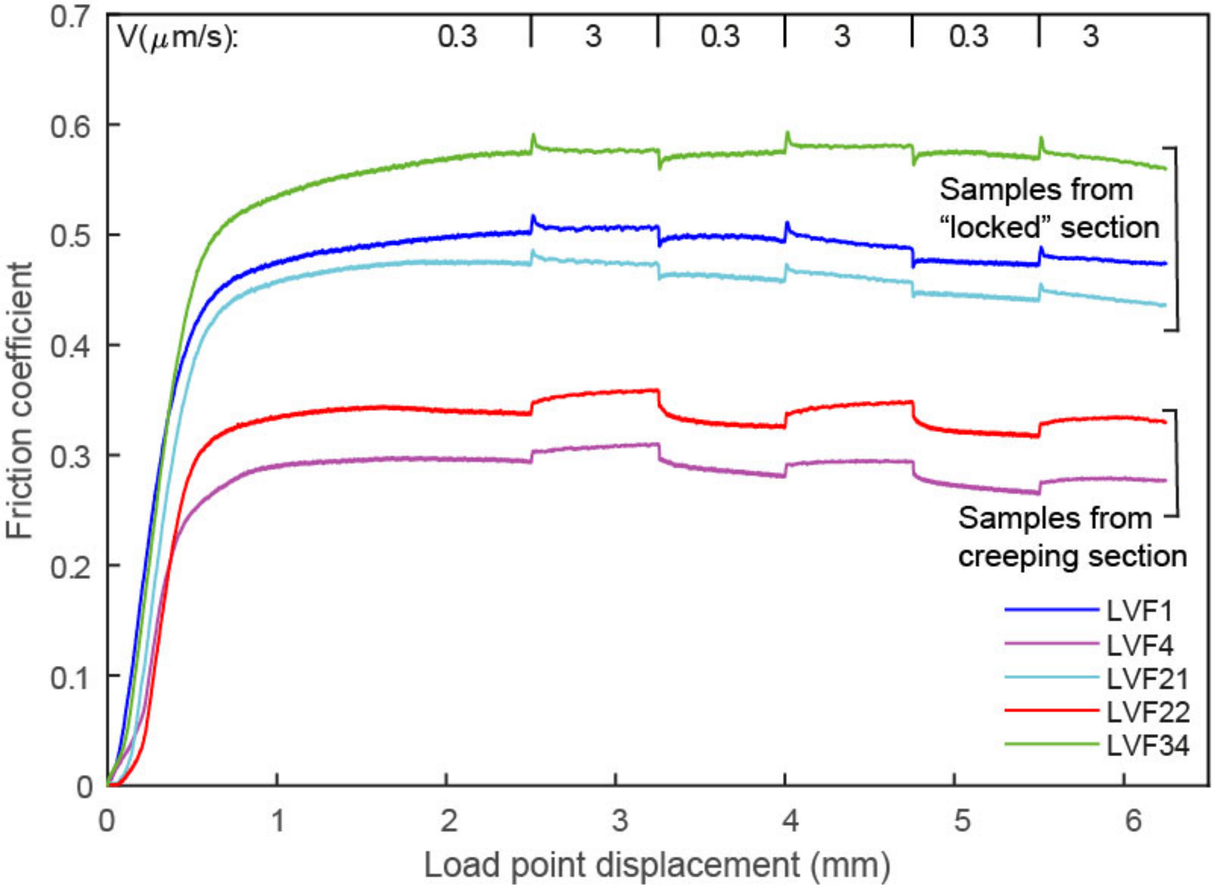
V(μm/s):
0.3
3
0.3
3
0.3
3
Friction coefficient
Load point displacement (mm)
Samples from "locked" section
Samples from creeping section
LVF1
LVF4
LVF21
LVF22
LVF34

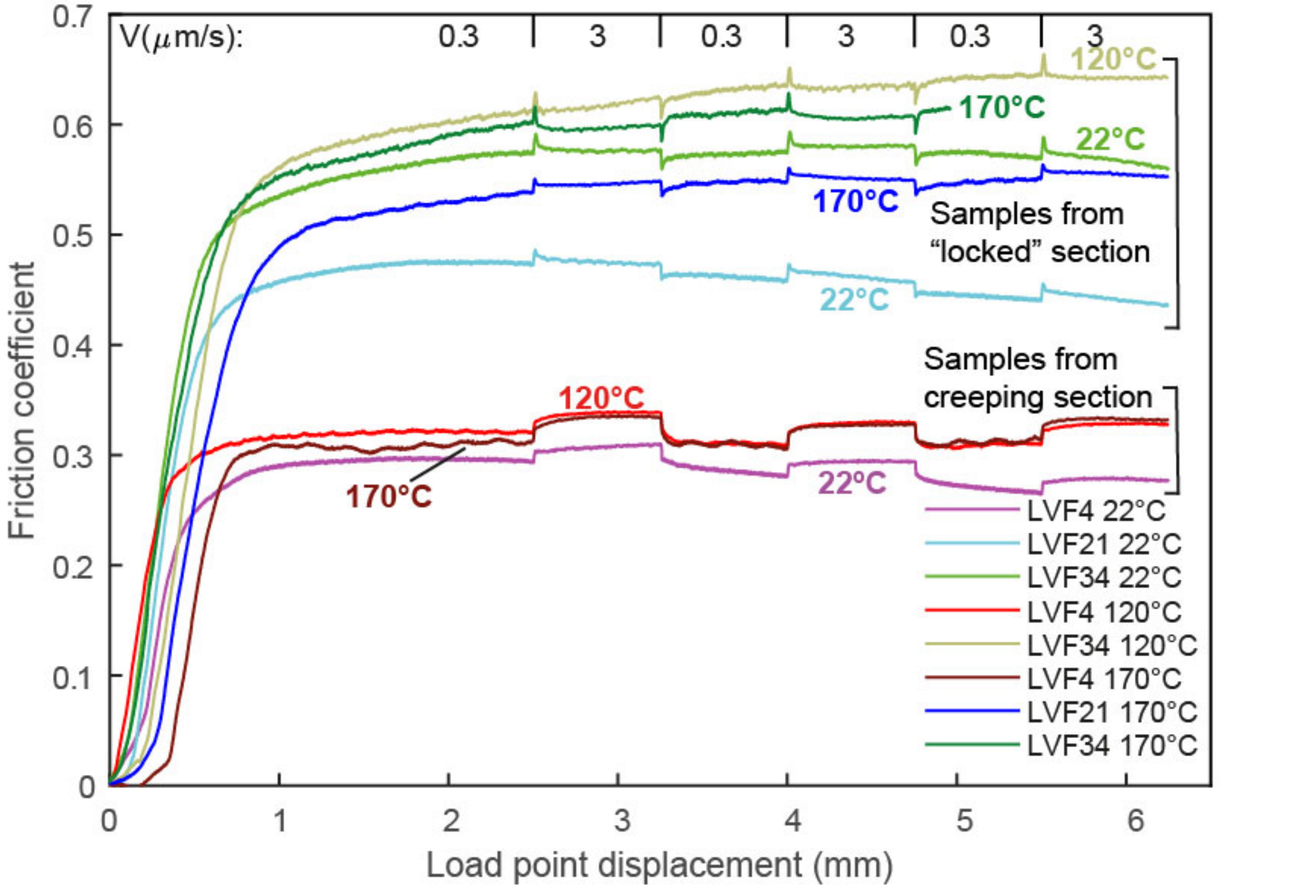
V(μm/s):
0.3
3
0.3
3
0.3
3
Friction coefficient
Load point displacement (mm)
120°C
170°C
22°C
170°C
22°C
Samples from "locked" section
120°C
170°C
22°C
Samples from creeping section
LVF4 22°C
LVF21 22°C
LVF34 22°C
LVF4 120°C
LVF34 120°C
LVF4 170°C
LVF21 170°C
LVF34 170°C

Figure3.

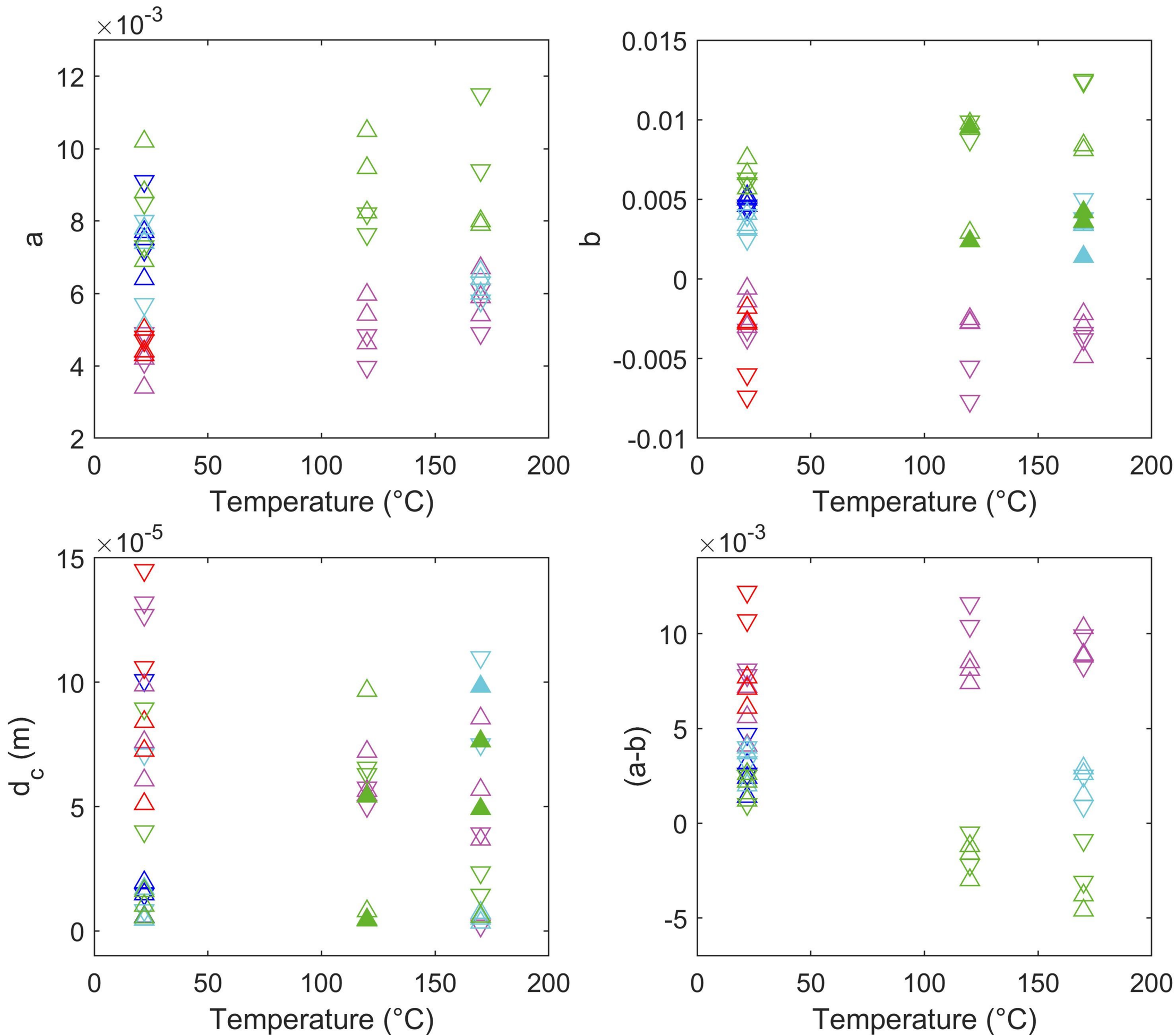
×10-3
12
10
8
6
4
2
a
0
50
100
150
200
Temperature (°C)
0.015
0.01
0.005
0
-0.005
-0.01
b
Temperature (°C)
LVF1
LVF4
LVF21
LVF22
LVF34
×10-5
15
10
5
0
dc (m)
Temperature (°C)
×10-3
10
5
0
-5
(a-b)
Temperature (°C)

Figure4.

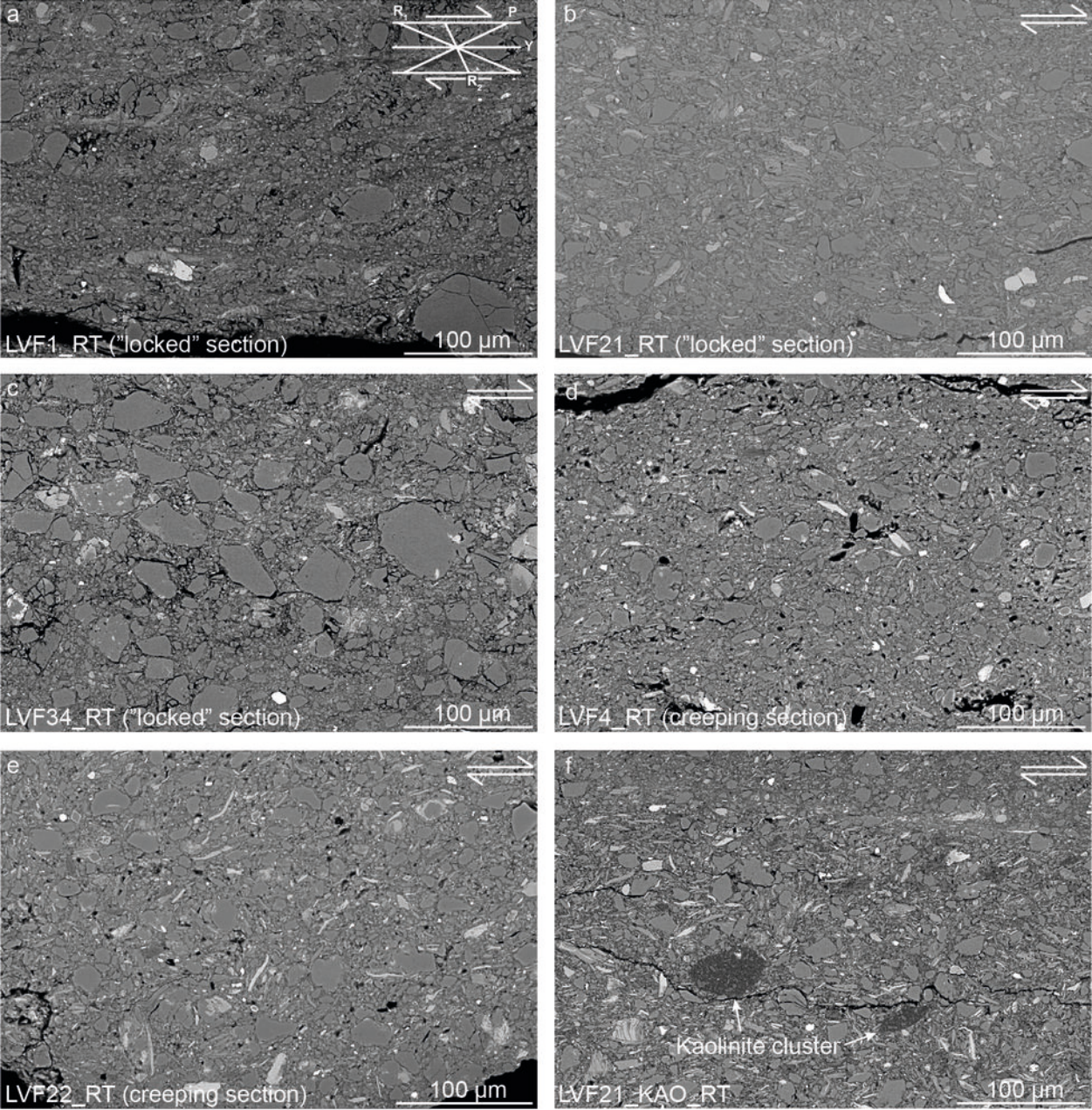
a
R1
P
Y
R2
LVF1_RT ("locked" section)
100 µm
b
LVF21_RT ("locked" section)
100 µm
c
LVF34_RT ("locked" section)
100 µm
d
LVF4_RT (creeping section)
100 µm
e
LVF22_RT (creeping section)
100 µm
f
Kaolinite cluster
LVF21_KAO_RT
100 µm

Figure5.

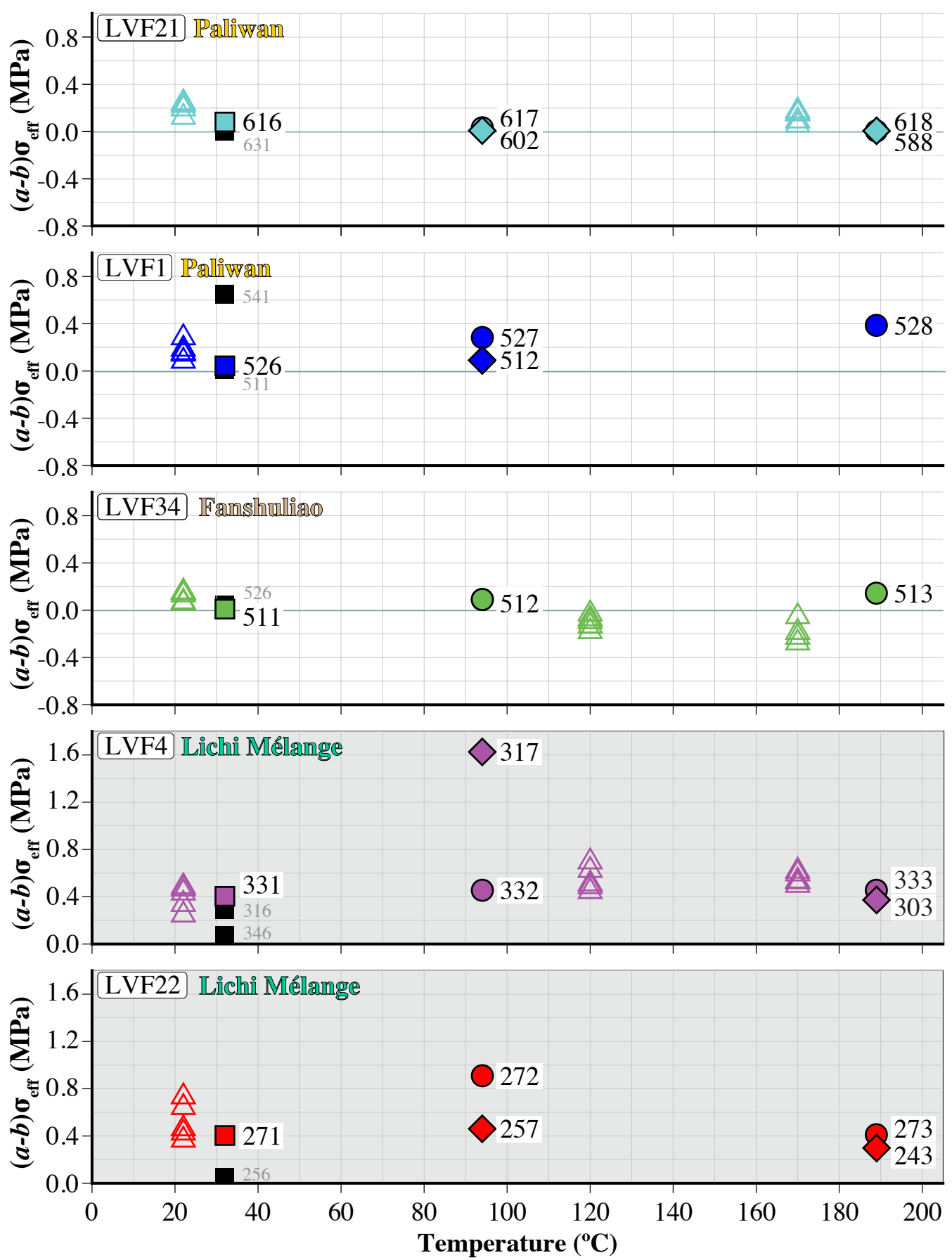
LVF21 Paliwan
LVF1 Paliwan
LVF34 Fanshuliao
LVF4 Lichi Mélange
LVF22 Lichi Mélange
(a-b)σeff (MPa)
Temperature (°C)
0 20 40 60 80 100 120 140 160 180 200
616
631
617
602
618
588
541
526
511
527
512
528
526
511
512
513
317
331
316
346
332
333
303
272
271
256
257
273
243

Figure6.

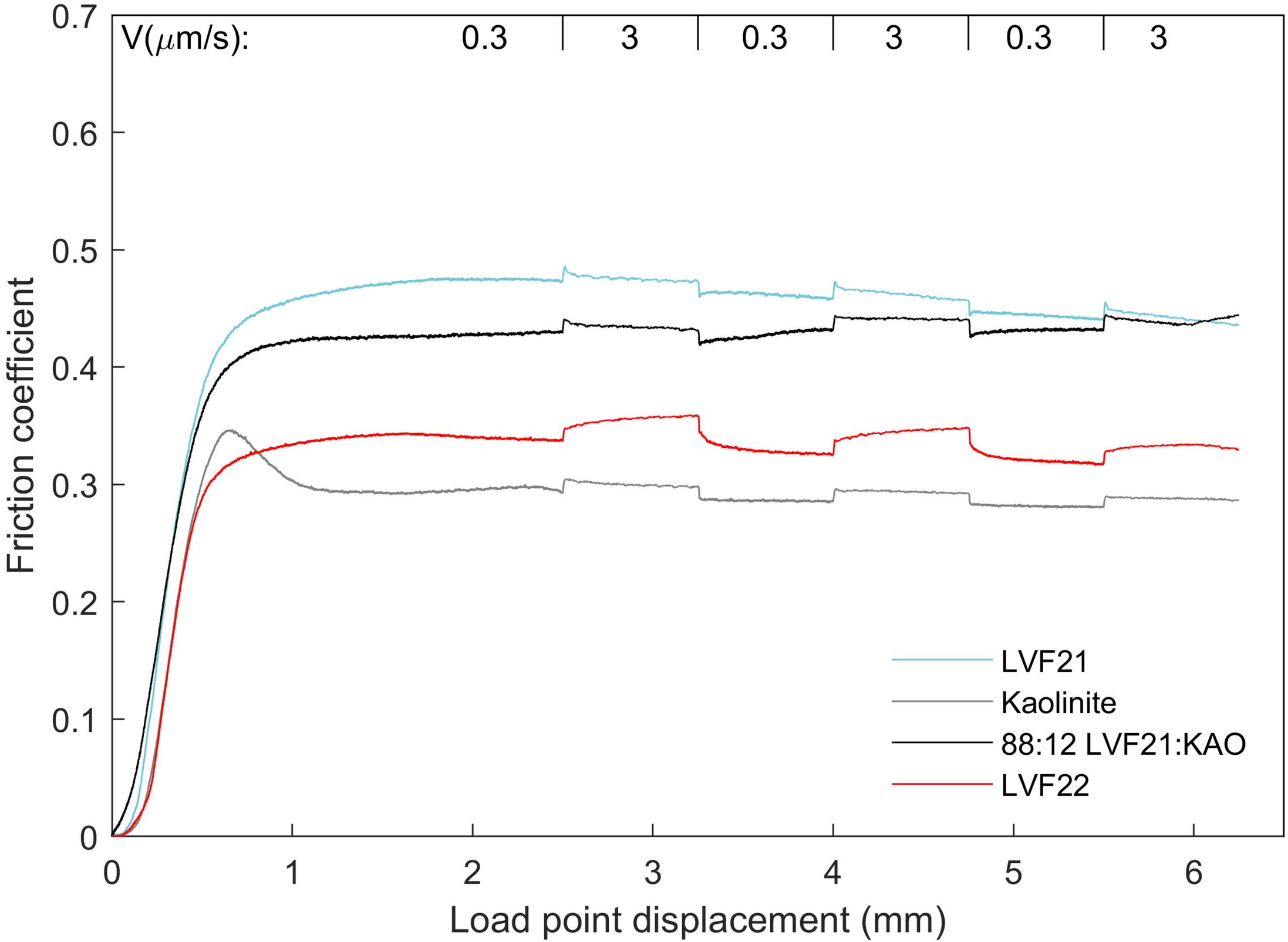
V(μm/s):
0.3
3
0.3
3
0.3
3
Friction coefficient
0.7
0.6
0.5
0.4
0.3
0.2
0.1
0
0
1
2
3
4
5
6
Load point displacement (mm)
LVF21
Kaolinite
88:12 LVF21:KAO
LVF22